Low-loss Plasmonic Dielectric Nanoresonators

Yi Yang,[*,†] Owen D. Miller,[*,‡] Thomas Christensen,[†] John D. Joannopoulos,[†] and Marin Soljačić[†]

[†]*Research Laboratory of Electronics, Massachusetts Institute of Technology, Cambridge, Massachusetts 02139, USA*

[‡]*Department of Applied Physics, Yale University, New Haven, CT 06520, USA*

E-mail: yiy@mit.edu; owen.miller@yale.edu

Abstract

Material losses in metals are a central bottleneck in plasmonics for many applications. Here we propose and theoretically demonstrate that metal losses can be successfully mitigated with dielectric particles on metallic films, giving rise to hybrid dielectric–metal resonances. In the far field, they yield strong and efficient scattering, beyond even the theoretical limits of all-metal and all-dielectric structures. In the near field, they offer high-Purcell-factor (>5000), high-quantum-efficiency (>90%), and highly directional emission at visible and infrared wavelengths. Their quality factors can be readily tailored from plasmonic-like (∼10) to dielectric-like (∼10^3), with wide control over the individual resonant coupling to photon, plasmon, and dissipative channels. Compared with conventional plasmonic nanostructures, such resonances show robustness against detrimental nonlocal effects and provide higher field enhancement at extreme nanoscopic sizes and spacings. These hybrid resonances equip plasmonics with high efficiency, which has been the predominant goal since the field's inception.

Keywords

nanoparticles, nanoantennas, radiative efficiency, light scattering, spontaneous emission, nonlocality

The material composition of an optical nanoresonator dictates sharply contrasting properties: metallic nanoparticles[1–6] support highly subwavelength plasmons with large field strengths, but which suffer from intrinsic material losses[7–11], whereas dielectric nanoparticles [12–15] support exquisite low-loss versatility, but only moderate confinement as their sizes must generally be wavelength-scale or larger. In this Letter, we propose and theoretically demonstrate that a combined approach—dielectric nanoparticles on metallic films—can exhibit a unique combination of strong fields and high confinement alongside small dissipative losses. We show the utility of such hybrid plasmonic dielectric resonators for (i) far-field excitations, where subwavelength silicon-on-silver nanoparticles can scatter more efficiently than is even theoretically possible for any all-metal or all-dielectric approach, and (ii) near-field excitations, where highly directional spontaneous emission enhancements >5000 are possible with quantum efficiencies >90% and even approaching unity. Moreover, the dielectric composition of the nanoparticle, when placed atop a metallic supporting film, should mitigate much of the quantum- and surface-induced nonlocal damping that occurs at nanometer scales, an effect we confirm quantitatively with a hydrodynamic susceptibility model. Furthermore, as our approach does not rely on nanostructured metallic components, it strongly constrains parasitic dissipation arising from fabrication imperfections. More broadly, simple geometrical variations provide wide control over the individual resonant-coupling rates to photon, plasmon, and dissipative degrees of freedom, opening a pathway to low-loss, high-efficiency plasmonics.

Mitigating loss is a pivotal goal[16–19] in plasmonics. When nanoparticles interact with plane waves, their cross-sections are typically dominated by dissipative absorption. In the near field, large spontaneous-emission enhancements (Purcell factors) have been demonstrated[20–24] through mode-volume squeezing, but it has been typically accompanied by sub-50% quantum efficiencies at visible frequencies. In a recent paper[25] we showed that optically thin films enable one to break the 50% radiative-efficiency barrier in all-metal structures. A subsequent question that emerges is whether dielectric-like *near-unity* efficiency and large

plasmonic confinement can be simultaneously achieved. Previously proposed hybrid structures[26,27] with separate dielectric (director) and metal (feed) functionality exhibit better radiative efficiency, but at the cost of lower enhancements. This tradeoff suggests the notion that strong and efficient plasmonic antennas are only possible at infrared frequencies[16], where they behave akin to perfect conductors and "plasmonic" effects are minor. Quantum corrections in plasmonics [28–31], e.g. due to electron tunneling[32–34] and nonlocality[35–37], further limit the ultimate enhancement of plasmonic resonators.

The difficulty of achieving low-loss plasmons has led to the perception that high confinement is simply incompatible with low loss, as large fields near/in a metal surface may necessarily generate significant dissipation. This intuition has led to the burgeoning field of alternative plasmonic materials[19,38,39], whereby highly doped semiconductors or polar dielectrics ideally exhibit negative real permittivities with small imaginary (lossy) parts. There has been a complementary effort in all-dielectric nanoparticles[12–14] and metamaterials[14,15], but subwavelength resonances fundamentally require metallic components with negative permittivities[7,16,40]. Material engineering has also been proposed in the form of band engineering[41] and gain offsets[42]. The perceived confinement–loss tradeoff is rigorously correct for quasistatic plasmonic resonators[7], in which the desired resonant frequency directly sets the fraction of the field intensity that must reside within the lossy metal[7,43,44]. In closed non-radiative plasmonic systems, proper geometrical optimization of dielectric-metal waveguides can reduce propagation losses[45]; in open systems, the central unanswered question is whether their radiative coupling rates can be strongly increased such that radiation significantly exceeds near-field dissipative losses. Here we show that open resonators comprising high-index, low-loss nanoparticles on metallic films can simultaneously achieve high confinement and high radiative efficiencies, without significant dissipative loss.

Conceptual basis. We propose a hybrid dielectric–metal resonator [Fig. 1(a)] that mitigates restrictions from metal losses on plasmonic scattering, emission, and quality factors to a great extent. The cylindrical symmetry implies that resonances can be labeled with in-

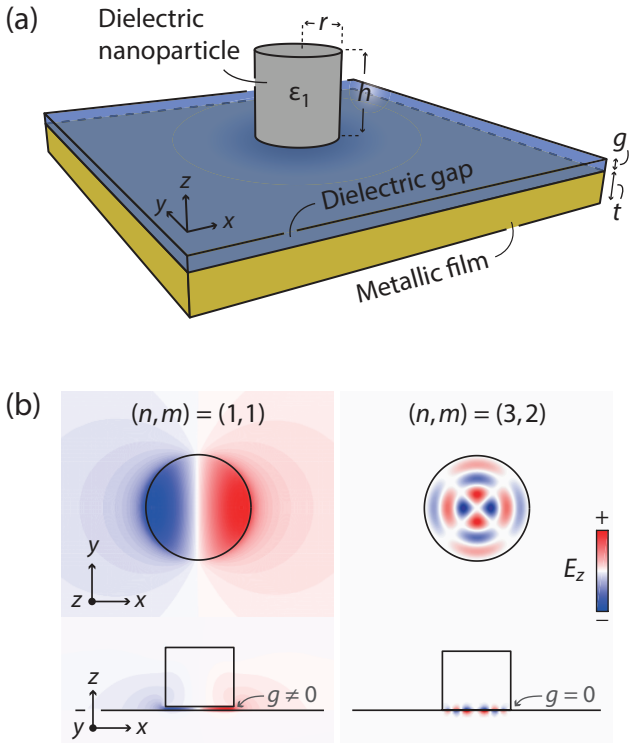

Figure 1: Hybrid dielectric–metal resonances. (a) Schematic of the structure, composed of a metallic layer of thickness t, a dielectric spacer with gap size g, and a dielectric cylindrical nanoparticle of permittivity ε_1, height h, and radius r. For simplicity, we here consider vacuum as the ambient and gap media. (b) E_z mode profiles of two selected hybrid resonances, for a Si cylinder on a Ag substrate. (Material parameters detailed in Supporting Info S1).

dices (n, m), enumerating field variations in the radial and azimuthal directions, respectively. Unlike the widely used all-metal "gap-plasmon" resonances[46–50] (hereafter, metal–metal resonances), which require a nonzero gap to squeeze the field inside due to their metal-antenna-like operation[4,51], the dielectric–metal resonances strongly confine the resonant field for either zero or nonzero gap [Fig. 1(b)].

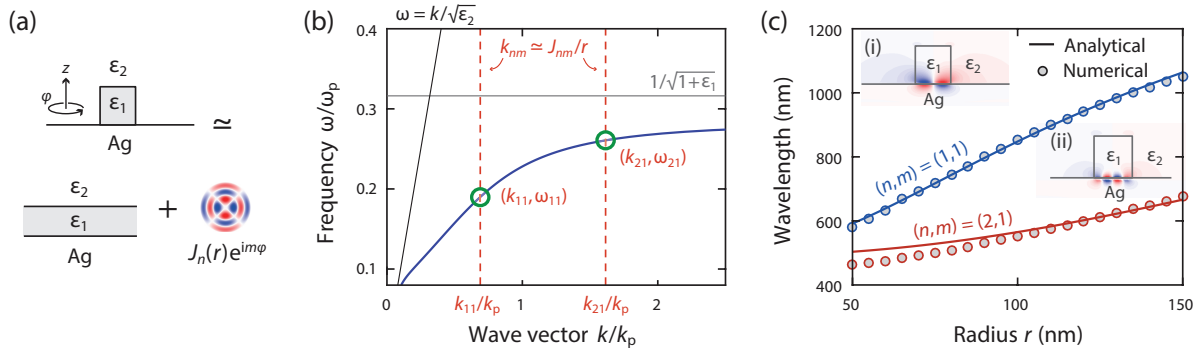

Figure 2: Analytical model of hybrid dielectric–metal resonances. (a) Pictorial representation of the hybrid resonance, which approximately satisfies a Bessel-function phase-matching condition, Eq. 1, imposed on the underlying planar structure. (b) The application of Eq. 1 illustrated in a concrete system ($h = 100\,\text{nm}$, with $\varepsilon_1 = 12.25$, $\varepsilon_2 = 1$, $t = \infty$, and $g = 0$): the underlying planar system's plasmon dispersion (blue) and the resonant wavevectors k_{nm} (red dashed) dictate resonant frequencies ω_{nm}. ω_p and k_p denote plasma frequency and $k_\text{p} = \omega_\text{p}/c$ (c being speed of light). (c) The resonant wavelengths of the $(1, 1)$ and $(2, 1)$ [E_z profiles shown in (i) and (ii) respectively] modes versus cylinder radius r, as predicted by Eq. (1) (solid lines) and numerical computations (circles).

Conceptually, the dielectric–metal resonances can be understood as the surface plasmons of a planar multilayer metal–dielectric system restricted to specific quantized wavevectors k_{nm}. The nanoparticle's boundary reflects surface plasmons of general wavevector k without phase shift. For a cylinder of radius r, the round-trip phase over the nanoparticle is given by the Bessel function of the first kind $J_n(kr)$. Localized resonances are supported when this round trip phase vanishes, i.e., at the Bessel zeros J_{nm}:

$$k_{nm} r \simeq J_{nm}. \tag{1}$$

Resonant frequencies are obtained by sampling the multilayer surface plasmon dispersion curve, $\omega(k)$, at the resonant wavevectors $k_{nm} \simeq J_{nm}/r$ [Fig. 2(b)], as verified by the agreement between analytics and numerics [Fig. 2(c)]. Eq. (1) is most accurate for low-order resonances, when the plasmon reflection phase[52] at the nanoparticle boundary is small ($\mathrm{Re}\, k \gg \mathrm{Im}\, k$). Eq. (1) is also generalizable to other nanoparticle geometries and more complex multilayers.

This simple, yet accurate picture of the hybrid resonances, as part-plasmon, part-Bessel resonances, illustrates the separation of key functionality: the plasmonic metal provides vertical confinement, while the dielectric provides horizontal confinement and dictates the resonant condition. External radiative coupling occurs at the low-loss dielectric–air interface, away from the lossy metal, enabling higher radiative efficiencies than those in conventional plasmonic nanostructures.

Far-field scattering. Metallic nanoparticles generally scatter more strongly than all-dielectric nanoparticles. Yet this large scattering strength—as measured, e.g., by the optical cross-section per unit particle volume—is typically accompanied by significant absorption. Thus for many applications where absorption is undesirable (such as photovoltaics[53,54]), the critical figure of merit is scattering strength accompanied by high radiative efficiency. Here we leverage recently developed optical-response bounds to show that low-loss dielectric nanoparticles on metallic films can achieve subwavelength scattering with large radiative efficiency, surpassing all-metal and all-dielectric scatterers and approaching fundamental limits.

There has been significant interest in finding general upper bounds to optical response[55,56], and recently we developed new such bounds[9–11]. Passivity, which requires non-negative absorbed and scattered powers, imposes limits to the currents that can be excited in an absorptive scatterer, leading to bounds that are independent of shape, which account for material loss ($\propto \mathrm{Im}\, \chi$, for material susceptibility χ), and which can incorporate radiative-efficiency constraints. The bounds demonstrate[10] that high radiative efficiency, defined as $\eta \equiv \sigma_{\mathrm{sca}}/(\sigma_{\mathrm{sca}} + \sigma_{\mathrm{abs}}) = \sigma_{\mathrm{sca}}/\sigma_{\mathrm{ext}}$ (where σ_{sca}, σ_{abs}, and σ_{ext} are the scattering, ab-

sorption, and extinction cross sections, respectively), necessarily reduces the largest cross-section per volume that can be achieved. A natural figure of merit ($\mathrm{FOM_{sca}}$) emerges: $\sigma_{\mathrm{sca}}/V \times 1/[\eta(1-\eta)]$ (equivalently, $\sigma_{\mathrm{ext}}/\sigma_{\mathrm{abs}} \times \sigma_{\mathrm{ext}}/V$), which rewards high scattering cross-section (σ_{sca}/V) as well as high radiative efficiency ($\eta \gg 0.5$). The $\mathrm{FOM_{sca}}$ is subject to the bound[10]

$$\mathrm{FOM_{sca}} \equiv \frac{\sigma_{\mathrm{sca}}/\mathrm{V}}{\eta\,(1-\eta)} \leq \frac{\omega}{\mathrm{c}} \frac{|\chi(\omega)|^2}{\mathrm{Im}\,\chi(\omega)} \frac{\mathrm{I_{inc}}}{\mathrm{I_0}}, \tag{2}$$

which depends only on the frequency ω, the material composition, and the incident field properties. I_{inc}/I_0 is the ratio of the incident-field intensity I_{inc} (including e.g., reflection from a planar film in the absence of the nanoparticle) integrated over particle volume to the intensity of the plane wave. Perfect radiative efficiency ($\eta = 1$) is unachievable for lossy scatterers, such that Eq. (2) cannot diverge. Equation (2) clearly shows that low-loss materials offer the possibility for strong and high-efficiency scattering, but all-dielectric structures cannot reach their bounds (in most parameter regimes) for lack of subwavelength resonances. On the other hand, by equipping dielectric nanoparticles with a subwavelength resonant mechanism, achieved by coupling to a metallic substrate, these high limits may actually be approached.

We compare scattering by three types of resonators—(i) a free-space, all-dielectric resonator, (ii) a hybrid dielectric-on-metal resonator, and (iii) a metal-on-metal resonator—at 700 nm wavelength. For each resonator, the dielectric is Si. The free-space dielectric resonator [Fig. 3(a)] is designed to achieve super-scattering[57] (Supporting Info S2), with $\eta \approx 96\%$, via aligned electric- and magnetic-dipole moments. The hybrid silicon-on-silver resonator [Fig. 3(b)] is optimized to have a similar scattering cross-section, which is achieved in roughly one-fifth of the volume and with $\eta \approx 93\%$. Finally, the radius of the Ag-on-Ag resonator [Fig. 3(c)] is optimized by radius [cylinder height and gap size same as Fig. 3(b) for constant I_{inc}]; notably, it only achieves only $\approx 17\%$ radiative efficiency. Figure 3(d)

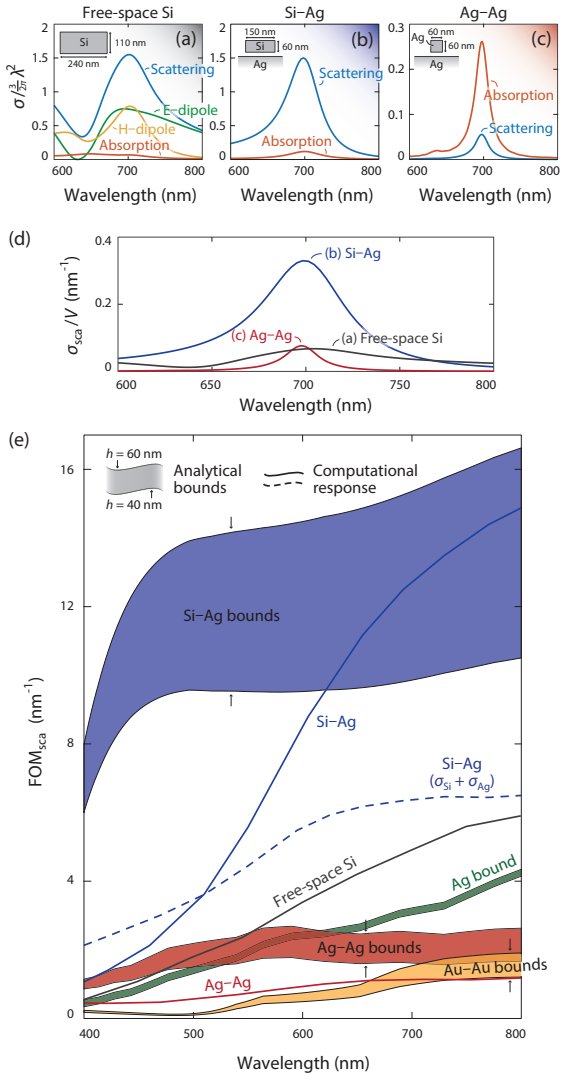

Figure 3: Dielectric–metal resonances offer strong scattering accompanied by modest absorption, at combined rates that cannot be achieved by all-metal or all-dielectric structures. Top: Scattering and absorption cross sections of nanoparticles under varying material and environment composition: (a) Si cylinder in free-space; (b-c) Si and Ag cylinders, respectively, above a semi-infinite Ag substrate with gap thickness $g = 2\,\text{nm}$. Geometrical parameters (insets) are chosen to align their resonant wavelengths at 700 nm. The three structures are all illuminated by normally-incident plane waves. In (b-c), the absorption includes the dissipation in both the particle and the substrate. (d) The dielectric–metal structure shows the highest per-volume scattering cross-section, because it simultaneously achieves large scattering cross-section σ_{sca}, high radiative efficiency η, and a small particle volume V. (e) In the visible regime, the scattering capabilities of metal–metal geometries (Ag–Ag and Au–Au bounds), free-space metallic (Ag bound), and free-space dielectric (Si free-space) scatterers all fall short when compared with the dielectric–metal (Si–Ag) scatterer, which also approaches its own upper bound, per Eq. (2). For the Si–Ag and Ag–Ag structures, the gap size is fixed at 5 nm; the cylinder (both Si and Ag) height h ranges from 40 nm to 60 nm in order to tune the resonant wavelength.

compares the scattering strengths of the three architectures, measured by σ_{sca}/V, clearly showing the dielectric–metal structure's advantage, which remains compelling across visible frequencies [Fig. 3(e)]. Fig. 3(e) compares FOM_{sca} of different structures and includes corresponding bounds (shaded regions) based on the cylinder height (Supporting Info S3) due to the oscillatory incident fields in the presence of the reflective film. Different from Fig. 3(a–d), all cross-sections in Fig. 3(e) (except the dashed line) isolate both the radiative and absorptive contributions of the nanoparticles from that of the underlying film: specifically, the nanoparticles define the scattering bodies while the substrates modify their environment and are incorporated into the definitions of the incident field (Supporting Info S4). This separation isolates the scattering properties of the nanoparticle, and is essential for many relevant applications. For example, to design nanoparticle scatterers for maximum light trapping in solar absorbers[53,54], it is crucial for the particles to have high radiative efficiency, whereas the absorber should operate in the opposite regime. At longer wavelengths, the scattering strength of the Si cylinder (blue solid line) approaches its bound, the highest among all bounds. By replacing the cylinder with a horizontally-aligned nanorod in the dielectric–metal system, scattering bounds can be saturated across the entire visible spectrum (Supporting Info Fig. S1). Including film absorption and scattering in the dielectric-metal structure (blue dashed line), the hybrid resonance retains large FOM_{sca}, still outperforming all-metal and all-dielectric resonators.

The hybrid resonators have two key advantages over all-dielectric resonators, beyond the FOM_{sca} comparison in Fig. 3(e). First, the hybrid resonators have tunable radiative efficiencies with commensurate tunability in their scattering strengths: for instance, if an application requires 80% efficiency instead of 90%, the hybrid structure can be tuned to 80% radiative-efficiency mark while simultaneously gaining a factor of two in scattering per volume (σ_{sca}/V). In contrast, no such trade-off mechanism is effective in purely dielectric structures. Second, while FOM_{sca} of Eq. 2 neatly captures the advantages of simultaneously large scattering strength and large radiative efficiency, it may overemphasize the relative

importance of near-unity radiative efficiencies. For many applications, the $\approx 93\%$ radiative efficiency of the hybrid structure as shown in Fig. 3(b) is practically equivalent to the $\approx 96\%$ radiative efficiency of the all-silicon structure of Fig. 3(a), and yet this modest difference translates into a factor of two relative reduction in $\mathrm{FOM_{sca}}$ as a consequence of the $\propto 1/(1-\eta)$ dependence of $\mathrm{FOM_{sca}}$. For $\eta \sim 1$, this dependence likely overstates the comparative benefits of radiative efficiency for most applications, skewing the assessment of the comparative benefits of all-dielectric resonators. In the following section, we translate this large-response, high-radiative-efficiency capability from the far field to the near field.

Near-field emission enhancements. Plasmonic losses are particularly acute in the near field, for sources in close proximity to the resonator, as the source readily accesses lossy channels that dissipate energy before it can escape into a propagating far-field photon or guided plasmon. In contrast, with negligible local dissipation, dielectric–metal resonances can provide high-Purcell, high-efficiency, and high-directionality spontaneous emission enhancements. A Purcell factor >5000 with quantum efficiency (including both photon and plasmon emission) >90% can be achieved in the optical regime. Whereas some previous work (e.g., Ref.[23]) has not distinguished between emission into guided plasmons and emission into radiating photons, we separate each contribution and show that a simple geometrical reconfiguration (increasing/reducing the metal-film thickness) can swing the emission rate from plasmon-dominant ($> 75\%$) to photon-dominant ($> 75\%$) or vice versa. Directional photon and plasmon emission can also be realized via high-order resonances.

We first demonstrate *photon* emission enhancement with a silicon cylinder on a semi-infinite Ag substrate, separated by a 2 nm gap [Fig. 4(a)]. Planar dispersion analysis (Supporting Info Fig. S2) suggests that this geometry should provide similar Purcell enhancement, and much higher quantum efficiency, as compared to a 5 nm-gap-size metal–metal structure. We decompose[58] the enhanced emission from a z-oriented dipole into far-field photon, guided plasmon, and local dissipative channels and obtain corresponding efficiencies (Supporting Info S7) [Fig. 4(b)]. The $(1,1)$ and $(1,2)$ modes achieve Purcell factors (total

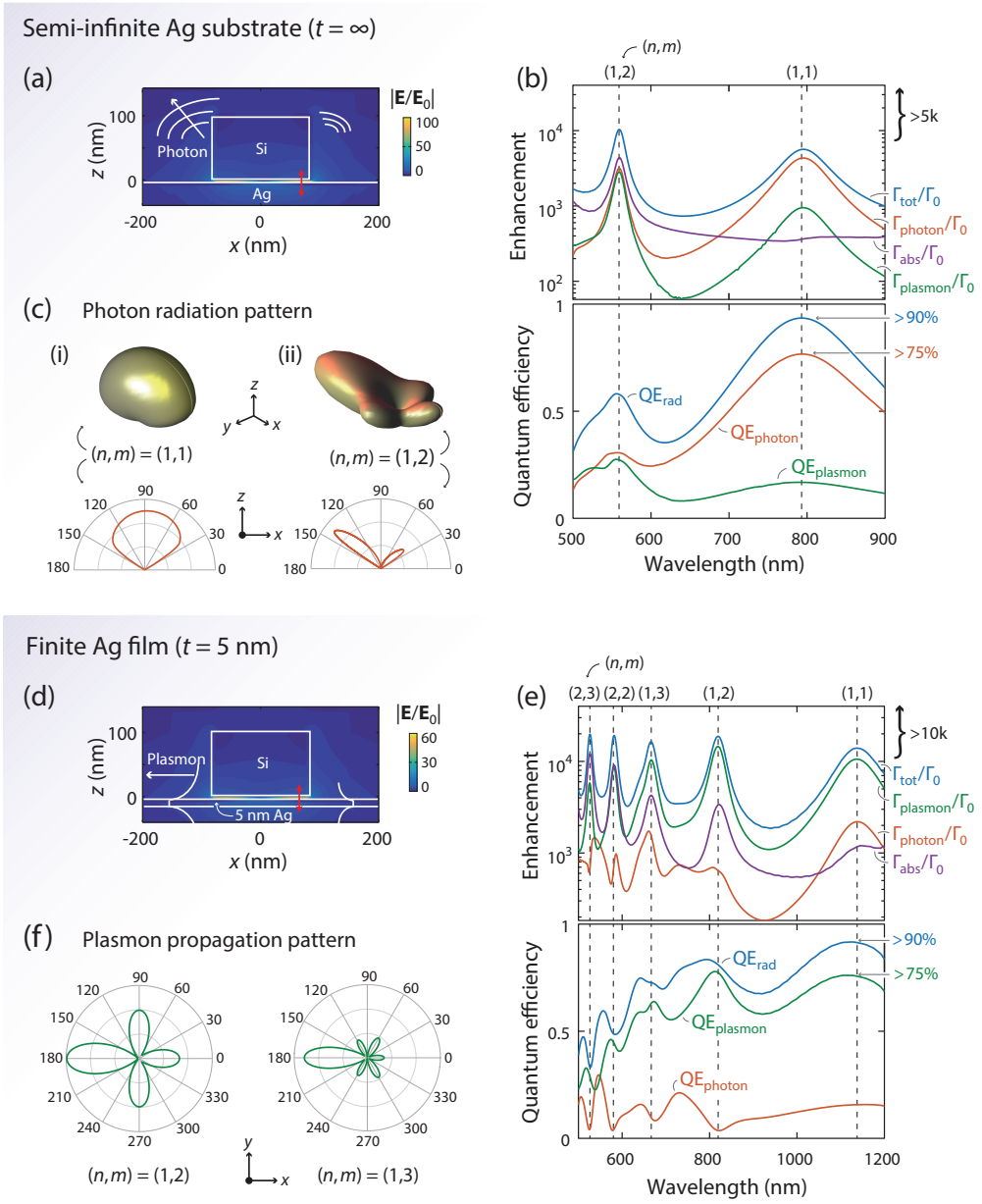

Figure 4: High-Purcell, high-efficiency, high-directionality spontaneous emission enhancement with the hybrid resonances. (a) Structure and its $(1,1)$ modal profile for photon emission. An $r = 80\,\text{nm}$, $h = 100\,\text{nm}$ silicon cylinder above semi-infinite Ag with a $g = 2$ nm gap. A z-oriented dipole (red arrow) is located in the middle of the gap and at $x = 67\,\text{nm}$. (b) Enhancement decomposition reveals strong and efficient photon emission. A high quantum efficiency >90% and photon efficiency >75% are achieved using the (1,1) mode. (c) Far-field photon radiation pattern of the $(1,1)$ and $(1,2)$ mode. Highly directional photon emission is achieved using the $(1,2)$ mode. (d) Structure and its $(1,1)$ resonance profile for plasmon emission. A finite-thickness ($t = 5$ nm) metallic film is considered; all other parameters mirror those in (a). (e) Enhancement decomposition reveals strong and efficient plasmon launching. The $(1,1)$ mode achieves a total radiative efficiency >90% and a plasmon efficiency >75%. (f) Directional plasmon propagation with the $(1,2)$ and $(1,3)$ mode.

enhancement) >5000 and $>10^4$, respectively. As importantly, the $(1,1)$ mode exhibits >90% quantum efficiency and >75% photon efficiency. Similar efficiencies are achieved for emitters located throughout the gap region (not shown; adopting the approach in[25]). In the far field [Fig. 4(c)], the $(1,1)$ mode exhibits wide-angle emission, while the $(1,2)$ mode enables highly directional photon emission, without the Yagi-Uda configuration[26,59] or a periodic lattice[60].

Even higher quantum efficiencies, with similar enhancements, are possible with alternative low-loss dielectric materials (on Ag). AlSb[61] nanoparticles offer close-to-unity efficiencies below their 2.2 eV direct bandgap. Ge nanoparticles exhibit Purcell factors of 2×10^4 with high radiative ($\approx 95\%$) and photon ($\approx 85\%$) efficiencies at the technologically relevant 1.55 µm wavelength (Supporting Info Fig. S3). Relative to a previously proposed[20] infrared antenna with similar efficiency, this Purcell factor is 10 times higher.

We further demonstrate *plasmon* generation[62] with high efficiency by using an optically thin ($t = 5$ nm) metal layer [Fig. 4(d)]. The thin metal improves the modal overlap between the gap and propagating plasmons[25]. The Purcell factors exceed 10^4 for all the modes in Fig. 4(e). Similar to the thick-metal case, high total quantum efficiencies are achieved, with that of the $(1,1)$ mode still >90%. Contrary to the thick-metal case, photon emission is suppressed while plasmon emission is strongly boosted: the plasmon efficiency exceeds 60% for each of the $(1,1)$, $(1,2)$ and $(1,3)$ modes. The guided-plasmon propagation pattern [Fig. 4(f)] reveals highly directional plasmon launching.

The use of ultra-thin metallic films is crucial to efficient plasmon generation due to the mode-overlap improvement between the gap and propagating plasmons[25]. It is similarly important for the material quality of the film to remain high at such nanometric thicknesses. Recent progress in thin-film synthesis, via low-temperature slow-speed (≈ 1 angstrom/minute) epitaxial growth[63] demonstrated the feasibility of fabricating pristine metallic films at ever-smaller thicknesses. Conversely, the choice of semi-infinite thickness for the substrates considered in this section for enhanced photon emission, and throughout the paper for near- and far-field enhancements, is primarily for simplicity and conceptual clarity. In practice,

the behavior of the resonator will be nearly identical for any film with a thickness exceeding silver's skin depth, $\gtrsim$ 30 nm; the substrate thickness can consequently be adapted as necessary for different experimental techniques or practical applications.

Widely Varying Quality Factors. The quasistatic properties of metals[7] limit the quality factors of conventional plasmonic resonances (typically <100 in the optical regime), imposing severe restrictions on many plasmonic applications. In contrast, dielectric–metal resonances provide control over the individual absorptive- and radiative-loss rates, providing options along the entire continuum between the all-metal and all-dielectric extremes.

Using approximately lossless dielectrics, such as TiO_2 at visible frequencies, plasmonic modes with extraordinarily high quality factors can be designed (Fig. 5). As evidenced by their field patterns [Fig. 5(a–b)], the modes of the dielectric–metal resonator partition into dielectric-like and plasmonic-like resonances—both of which display strong field confinement within the gap. Figure 5(c) shows the total, radiative, and absorptive quality factors (Q_{tot}, Q_{rad}, and Q_{abs}) of the resonances (Supporting Info S8). The dielectric-like modes generally have higher Q_{abs} than the plasmonic-like modes because of their larger field intensity in the interior of the dielectric [Fig. 5(a)]. Unlike conventional plasmonic modes, for which Q_{tot} is mainly limited by material loss, here Q_{tot} is primarily limited by radiation loss, which can be readily tailored via the nanoparticle geometry and size. The Q_{tot} of these resonances ranges widely from $\sim$10 to $\sim 10^3$, offering a wide, continuous design space for narrow- or broad-band plasmonic applications.

Robustness to Plasmonic Quantum Corrections. Quantum phenomena beyond the classical description set the ultimate limitations on the achievable response in plasmonic nanostructures. Chief among these phenomena are nonlocality, spill-out, and surface-enabled damping[28]. In Ag, their joint impacts are well-described by a nonlocal, effective model—GNOR[37] (Supporting Info S9), a convective-diffusive hydrodynamic model—causing spectral blueshifting and broadening in structures with nanoscale features. In comparison, analogous quantum corrections in dielectrics are negligible due to the absence of free carriers. We show

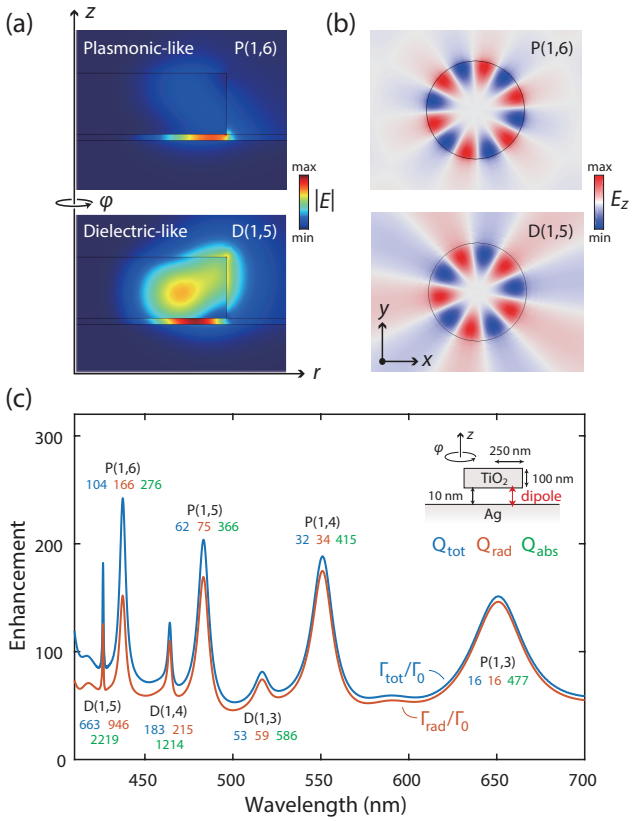

Figure 5: Low- and high-order (whispering-gallery-like) hybrid resonances offer a large continuous design space for plasmonic quality factors. (a–b) Field profiles of the plasmonic-like [P(1,6)] and dielectric-like [D(1,5)] resonances in the (a) r-z and (b) x-y planes. E_z are evaluated in the middle of the gap (particle) for the plasmonic-like (dielectric-like) resonance. (c) Total (blue), radiative (red), and absorptive (green) quality factors of the hybrid resonances. Inset: structure and dipole excitation for quality-factor extraction.

here that the dielectric–metal resonances display increased robustness to these detrimental quantum corrections compared to their metal–metal counterparts; taking field enhancement as a measure, the former is even superior for gaps $\lesssim 5\,\mathrm{nm}$.

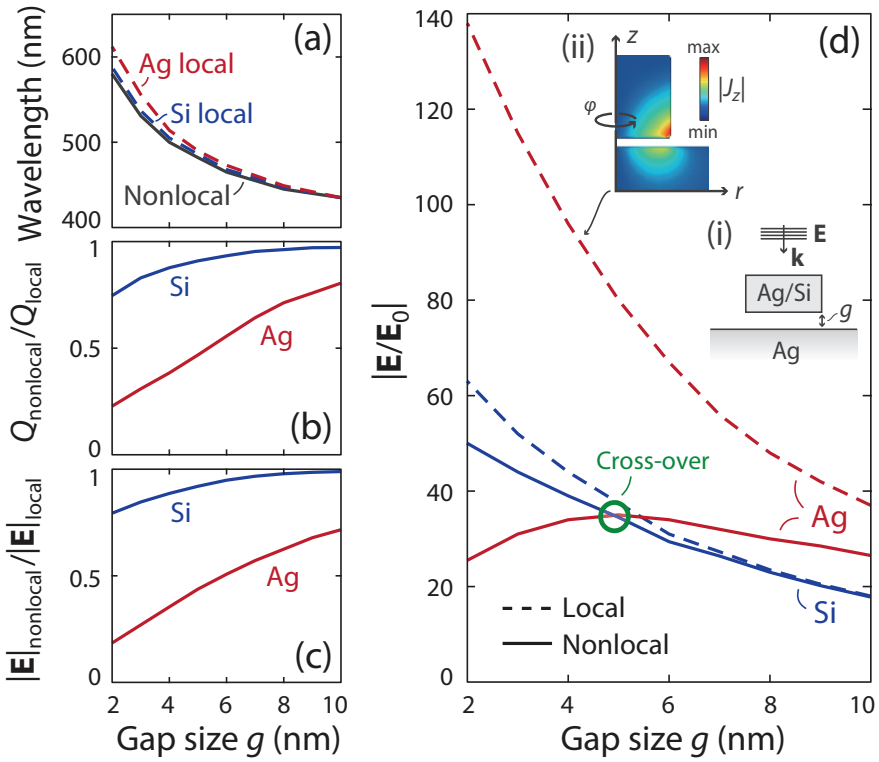

Figure 6: Hybrid resonances show increased robustness to the detrimental effects of quantum corrections than their metal–metal counterparts. The (1,1) resonances of Ag or Si nanocylinders above a semi-infinite Ag film, separated by a finite gap [inset (i)]. The radius (height) of the Si cylinder is 50 nm (40 nm). The Ag cylinder is of identical height but of variable radius, 24–34 nm, to spectrally align the distinct structures' (nonlocal) resonance wavelength. An effective nonlocal model[37] reveals that (a) spectral blueshifting, (b) linewidth broadening, and (c) field enhancement (at gap center) reduction, relative to classical (local) predictions, are greatly mitigated in the hybrid resonators relative to metal–metal resonators. (d) Accounting for nonlocal response, hybrid resonances exhibit higher field enhancement than the metal–metal resonance for gap sizes $\lesssim 5\,\mathrm{nm}$ (crossover in green marker). Inset (ii), the induced current distribution, $|J_z|$, of the metal–metal resonance (gap, $g = 4$ nm).

Figure 6 examines these quantum corrections for 2 nm to 10 nm gap sizes, where inter-surface electron tunneling is absent[29]. For both dielectric–metal and metal–metal structures (with equal nonlocal resonant frequencies), the resonant wavelength, quality factor, and field enhancement of the $(1, 1)$ resonance are shown [Fig. 6(a-c)] as functions of gap size. Relative

to local, classical predictions, both configurations exhibit blueshifted resonant wavelengths and reductions in quality factor and field enhancement—all of which increase as the gap size decreases. Crucially, the metal–metal system suffers more severe reductions than its counterpart. This observation can be attributed to two cooperating effects: first, in light of the plasmon–Bessel framework laid out above (Fig. 2), the planar multilayer equivalent approximately dictates the gap-dependent impact of quantum corrections. Accordingly, since the surface plasmon of the planar metal–dielectric–metal system suffers increased impact of quantum corrections compared to the planar dielectric–metal system (by a factor $1 + \mathrm{e}^{-kg\,31}$ and see Supporting Info Fig. S5), the metal–metal nanoparticle's performance is similarly reduced. Second, the metal nanoparticle's edges host sharply varying current densities [Fig. 6(d), inset (ii)] and consequently incur large nonlocal corrections in these regions.

Strikingly, the relative robustness of the hybrid resonances to quantum corrections enables them to demonstrate larger *absolute* field enhancements, for equal gap sizes $\lesssim 5\,\mathrm{nm}$ [Fig. 6(d)], than the high-intensity, pure-plasmonic metal–metal resonators. The enhancement in the latter system deteriorates drastically at these gap sizes, due to the above-noted distinguishing aspects. The comparative robustness of the hybrid resonances suggests a pathway to stronger light–matter interactions in extreme nanoscale gaps[64].

Discussion. In this Letter, we have shown the possibility for low-loss plasmonics by coupling low-loss dielectric nanoparticles with high-confinement metallic substrates. The hybrid dielectric–metal resonances exhibit strong and efficient scattering and near-field emission enhancements, large quality factors, and nonlocal robustness beyond those of conventional plasmonic nanostructures. The combined advantages of high-confinement and near-unity radiative efficiency make the hybrid platform an ideal candidate for a broad range of plasmonic applications, such as fluorescence[65], photovoltaics[53,54], sensing[66], and metasurfaces[67].

By avoiding any *structured* metallic components, the architecture has practical fabrication advantages. Single- or poly-crystalline metallic films exhibit much lower losses[63,68]

than metallic nanoparticles (which are typically amorphous, with more severe surface roughness). Moreover, this approach avoids the use of any metallic corners or tips that may strongly absorb due to fabrication imperfections. The dielectric particles considered here can be synthesized in colloidal form[69] and subsequently deposited or, alternatively, can be lithographically defined in situ[70].

The approach to high efficiency presented here can work in tandem with future material improvements. Just as we have shown that re-architecting common materials can improve their plasmonic response, new, low-loss materials should be integrated into these hybrid geometries rather than conventional all-metal structures. Graphene sheets behave optically very much like ultrathin metallic films, and thus our approach extends to dielectric-on-graphene architectures for efficient graphene plasmon confinement.

Looking forward, the dielectric-metal approach prompts two directions for new exploration. First, the strong emission enhancement of the dielectric–metal resonances rely on the high index contrast between the dielectric scatterer and the dielectric spacer (comprising the gap). When the index contrast is reduced, the high efficiencies can be maintained though at the expense of reduced optical confinement. Thus continued development of very-low-index ($n \approx 1$) materials, such as low-index SiO_2[71], aerogels[72], and low-index polymers[73], would further increase enhancements and improve efficiencies. Second, quantum effects in dielectric and dielectric–metal structures at few-nanometer length scales are of increasing interest, and should be explored further with alternative (e.g., time-dependent density functional theory) electronic and optical models. The prospect of dielectric–metal structures that are robust to deleterious nonlocal effects is especially enticing for the growing field of quantum plasmonics[74].

Acknowledgements

The authors thank fruitful discussions with Prof. Koppens and Dr. Bo Zhen. This work was partly supported by the Army Research Office through the Institute for Soldier Nanotechnologies under contract No. W911NF-13-D-0001. Y.Y. was partly supported by the MRSEC Program of the National Science Foundation under Grant No. DMR-1419807. O.D.M. was supported by the Air Force Office of Scientific Research under award number FA9550-17-1-0093. T.C. was supported by the Danish Council for Independent Research (Grant No. DFFC6108-00667). M.S. was partly supported (reading and analysis of the manuscript) by S3TEC, an Energy Frontier Research Center funded by the U.S. Department of Energy under grant no. DE-SC0001299.

Supporting Information Available

The Supporting Information is available free of charge on the ACS Publications website.

Bulk material parameters; Spherical harmonics decomposition; Scattering upper bound for a scatterer near a substrate; Scattering and absorption of the entire particle-substrate system and of the particle alone; Bound-saturated scattering realized via silicon nanorod on a silver film; Confinement and dissipative loss of dielectric-dielectric-metal (DDM) and metal-dielectric-metal (MDM) waveguides; Decomposition and far-field patterns of plasmon and photon emission; Quality factor decomposition; Generalized nonlocal optical response.

References

(1) Novotny, L.; Van Hulst, N. *Nat. Photonics* **2011**, *5*, 83–90.

(2) Giannini, V.; Fernández-Domínguez, A. I.; Heck, S. C.; Maier, S. A. *Chem. Rev.* **2011**, *111*, 3888–3912.

(3) Biagioni, P.; Huang, J.-S.; Hecht, B. *Rep. Prog. Phys.* **2012**, *75*, 024402.

(4) Tsakmakidis, K. L.; Boyd, R. W.; Yablonovitch, E.; Zhang, X. *Opt. Express* **2016**, *24*, 17916–17927.

(5) Kern, J.; Kullock, R.; Prangsma, J.; Emmerling, M.; Kamp, M.; Hecht, B. *Nature Photon.* **2015**, *9*, 582–586.

(6) Celebrano, M.; Wu, X.; Baselli, M.; Großmann, S.; Biagioni, P.; Locatelli, A.; De Angelis, C.; Cerullo, G.; Osellame, R.; Hecht, B.; Duò, L.; Ciccacci, F.; Finazzi, M. *Nature Nanotechnol.* **2015**, *10*, 412–417.

(7) Wang, F.; Shen, Y. R. *Phys. Rev. Lett.* **2006**, *97*, 206806.

(8) Shahbazyan, T. V. *Phys. Rev. Lett.* **2016**, *117*, 207401.

(9) Miller, O. D.; Hsu, C. W.; Reid, M. T. H.; Qiu, W.; DeLacy, B. G.; Joannopoulos, J. D.; Soljačić, M.; Johnson, S. G. *Phys. Rev. Lett.* **2014**, *112*, 123903.

(10) Miller, O. D.; Polimeridis, A. G.; Reid, M. H.; Hsu, C. W.; DeLacy, B. G.; Joannopoulos, J. D.; Soljačić, M.; Johnson, S. G. *Opt. Express* **2016**, *24*, 3329–3364.

(11) Miller, O. D.; Johnson, S. G.; Rodriguez, A. W. *Phys. Rev. Lett.* **2015**, *115*, 204302.

(12) Krasnok, A. E.; Miroshnichenko, A. E.; Belov, P. A.; Kivshar, Y. S. *Opt. Express* **2012**, *20*, 20599–20604.

(13) Fu, Y. H.; Kuznetsov, A. I.; Miroshnichenko, A. E.; Yu, Y. F.; Lukyanchuk, B. *Nat. Commun.* **2013**, *4*, 1527.

(14) Kuznetsov, A. I.; Miroshnichenko, A. E.; Brongersma, M. L.; Kivshar, Y. S.; Luk'yanchuk, B. *Science* **2016**, *354*, 846.

(15) Jahani, S.; Jacob, Z. *Nat. Nanotechnol.* **2016**, *11*, 23–36.

(16) Khurgin, J. B. *Nat. Nanotechnol.* **2015**, *10*, 2–6.

(17) Tassin, P.; Koschny, T.; Kafesaki, M.; Soukoulis, C. M. *Nat. Photon.* **2012**, *6*, 259–264.

(18) Boltasseva, A.; Atwater, H. A. *Science* **2011**, *331*, 290–291.

(19) Naik, G. V.; Shalaev, V. M.; Boltasseva, A. *Adv. Mater.* **2013**, *25*, 3264–3294.

(20) Rogobete, L.; Kaminski, F.; Agio, M.; Sandoghdar, V. *Opt. Lett.* **2007**, *32*, 1623–1625.

(21) Kinkhabwala, A.; Yu, Z.; Fan, S.; Avlasevich, Y.; Müllen, K.; Moerner, W. *Nat. Photon.* **2009**, *3*, 654–657.

(22) Russell, K. J.; Liu, T.-L.; Cui, S.; Hu, E. L. *Nat. Photon.* **2012**, *6*, 459–462.

(23) Akselrod, G. M.; Argyropoulos, C.; Hoang, T. B.; Ciracì, C.; Fang, C.; Huang, J.; Smith, D. R.; Mikkelsen, M. H. *Nat. Photon.* **2014**, *8*, 835–840.

(24) Eggleston, M. S.; Messer, K.; Zhang, L.; Yablonovitch, E.; Wu, M. C. *Proc. Natl. Acad. Sci.* **2015**, *112*, 1704–1709.

(25) Yang, Y.; Zhen, B.; Hsu, C. W.; Miller, O. D.; Joannopoulos, J. D.; Soljačić, M. *Nano Lett.* **2016**, *16*, 4110–4117.

(26) Devilez, A.; Stout, B.; Bonod, N. *ACS Nano* **2010**, *4*, 3390–3396.

(27) Rusak, E.; Staude, I.; Decker, M.; Sautter, J.; Miroshnichenko, A. E.; Powell, D. A.; Neshev, D. N.; Kivshar, Y. S. *Appl. Phys. Lett.* **2014**, *105*, 221109.

(28) Feibelman, P. J. *Prog. Surf. Sci.* **1982**, *12*, 287–407.

(29) Zhu, W.; Esteban, R.; Borisov, A. G.; Baumberg, J. J.; Nordlander, P.; Lezec, H. J.; Aizpurua, J.; Crozier, K. B. *Nat. Commun.* **2016**, *7*, 11495.

(30) Varas, A.; García-González, P.; Feist, J.; García-Vidal, F. J.; Rubio, A. *Nanophotonics* **2016**, 409.

(31) Christensen, T.; Yan, W.; Jauho, A.-P.; Soljačić, M.; Mortensen, N. A. *Phys. Rev. Lett.* **2017**, *118*, 157402.

(32) Esteban, R.; Borisov, A. G.; Nordlander, P.; Aizpurua, J. *Nat. Commun.* **2012**, *3*, 825.

(33) Savage, K. J.; Hawkeye, M. M.; Esteban, R.; Borisov, A. G.; Aizpurua, J.; Baumberg, J. J. *Nature* **2012**, *491*, 574–577.

(34) Scholl, J. A.; García-Etxarri, A.; Koh, A. L.; Dionne, J. A. *Nano Lett.* **2013**, *13*, 564–569.

(35) García de Abajo, F. J. *J. Phys. Chem. C* **2008**, *112*, 17983–17987.

(36) Ciracì, C.; Hill, R.; Mock, J.; Urzhumov, Y.; Fernández-Domínguez, A.; Maier, S.; Pendry, J.; Chilkoti, A.; Smith, D. *Science* **2012**, *337*, 1072–1074.

(37) Mortensen, N. A.; Raza, S.; Wubs, M.; Søndergaard, T.; Bozhevolnyi, S. I. *Nat. Commun.* **2014**, *5*, 3809.

(38) West, P. R.; Ishii, S.; Naik, G. V.; Emani, N. K.; Shalaev, V. M.; Boltasseva, A. *Laser Photonics Rev.* **2010**, *4*, 795–808.

(39) Khurgin, J. B. *Phil. Trans. R. Soc. A* **2017**, *375*, 20160068.

(40) Ammari, H.; Ciraolo, G.; Kang, H.; Lee, H.; Milton, G. W. *Arch. Ration. Mech. Anal.* **2013**, *208*, 667–692.

(41) Khurgin, J. B.; Sun, G. *Appl. Phys. Lett.* **2010**, *96*, 181102.

(42) Zayats, A. V.; Maier, S. A. *Active plasmonics and tuneable plasmonic metamaterials*; Wiley Online Library, 2013.

(43) Raman, A.; Shin, W.; Fan, S. *Phys. Rev. Lett.* **2013**, *110*, 183901.

(44) Khurgin, J. B.; Boltasseva, A. *MRS Bull.* **2012**, *37*, 768–779.

(45) Oulton, R. F.; Sorger, V. J.; Genov, D.; Pile, D.; Zhang, X. *Nat. Photon.* **2008**, *2*, 496–500.

(46) Esteban, R.; Teperik, T.; Greffet, J.-J. *Phys. Rev. Lett.* **2010**, *104*, 026802.

(47) Moreau, A.; Ciracì, C.; Mock, J. J.; Hill, R. T.; Wang, Q.; Wiley, B. J.; Chilkoti, A.; Smith, D. R. *Nature* **2012**, *492*, 86–89.

(48) Belacel, C.; Habert, B.; Bigourdan, F.; Marquier, F.; Hugonin, J.-P.; de Vasconcellos, S. M.; Lafosse, X.; Coolen, L.; Schwob, C.; Javaux, C.; Dubertret, B.; Greffet, J.-J.; Senellart, P.; Maitre, A. *Nano Lett.* **2013**, *13*, 1516–1521.

(49) Rose, A.; Hoang, T. B.; McGuire, F.; Mock, J. J.; Ciracì, C.; Smith, D. R.; Mikkelsen, M. H. *Nano Lett.* **2014**, *14*, 4797–4802.

(50) Faggiani, R.; Yang, J.; Lalanne, P. *ACS Photon.* **2015**, *2*, 1739–1744.

(51) Bowen, P. T.; Smith, D. R. *Phys. Rev. B* **2014**, *90*, 195402.

(52) Gordon, R. *Phys. Rev. B* **2006**, *73*, 153405.

(53) Atwater, H. A.; Polman, A. *Nat. Mater.* **2010**, *9*, 205–213.

(54) Brongersma, M. L.; Cui, Y.; Fan, S. *Nature Materials* **2014**, *13*, 451–460.

(55) Gustafsson, M.; Sohl, C.; Kristensson, G. *Proc. R. Soc. A* **2007**, *463*, 2589–2607.

(56) Hugonin, J.-P.; Besbes, M.; Ben-Abdallah, P. *Phys. Rev. B* **2015**, *91*, 180202.

(57) Ruan, Z.; Fan, S. *Phys. Rev. Lett.* **2010**, *105*, 013901.

(58) Yang, J.; Hugonin, J.-P.; Lalanne, P. *ACS Photon.* **2016**, *3*, 395–402.

(59) Curto, A. G.; Volpe, G.; Taminiau, T. H.; Kreuzer, M. P.; Quidant, R.; van Hulst, N. F. *Science* **2010**, *329*, 930–933.

(60) Lozano, G.; Louwers, D. J.; Rodríguez, S. R.; Murai, S.; Jansen, O. T.; Verschuuren, M. A.; Rivas, J. G. *Light: Sci. Appl.* **2013**, *2*, e66.

(61) Zollner, S.; Lin, C.; Schönherr, E.; Böhringer, A.; Cardona, M. *J. Appl. Phys.* **1989**, *66*, 383–387.

(62) Gan, C. H.; Hugonin, J.-P.; Lalanne, P. *Phys. Rev. X* **2012**, *2*, 021008.

(63) Wu, Y.; Zhang, C.; Estakhri, N. M.; Zhao, Y.; Kim, J.; Zhang, M.; Liu, X.-X.; Pribil, G. K.; Alù, A.; Shih, C.-K.; Li, X. *Adv. Mater.* **2014**, *26*, 6106–6110.

(64) Chikkaraddy, R.; de Nijs, B.; Benz, F.; Barrow, S. J.; Scherman, O. A.; Rosta, E.; Demetriadou, A.; Fox, P.; Hess, O.; Baumberg, J. J. *Nature* **2016**, *535*, 127–130.

(65) Tam, F.; Goodrich, G. P.; Johnson, B. R.; Halas, N. J. *Nano Lett.* **2007**, *7*, 496–501.

(66) Anker, J. N.; Hall, W. P.; Lyandres, O.; Shah, N. C.; Zhao, J.; Van Duyne, R. P. *Nat. Mater.* **2008**, *7*, 442–453.

(67) Huang, L.; Chen, X.; Mühlenbernd, H.; Zhang, H.; Chen, S.; Bai, B.; Tan, Q.; Jin, G.; Cheah, K.-W.; Qiu, C.-W.; Li, J.; Zentgraf, T.; Zhang, S. *Nat. Commun.* **2013**, *4*, 2808.

(68) McPeak, K. M.; Jayanti, S. V.; Kress, S. J.; Meyer, S.; Iotti, S.; Rossinelli, A.; Norris, D. J. *ACS Photon.* **2015**, *2*, 326–333.

(69) Fojtik, A.; Henglein, A. *Chem. Phys. Lett.* **1994**, *221*, 363–367.

(70) Person, S.; Jain, M.; Lapin, Z.; Sáenz, J.; Wicks, G.; Novotny, L. *Nano Lett.* **2013**, *13*, 1806–1809.

(71) Xi, J.-Q.; Schubert, M. F.; Kim, J. K.; Schubert, E. F.; Chen, M.; Lin, S.-Y.; Liu, W.; Smart, J. A. *Nat. Photon.* **2007**, *1*, 176–179.

(72) Sun, Y.; Forrest, S. R. *Nat. Photon.* **2008**, *2*, 483–487.

(73) Groh, W.; Zimmermann, A. *Macromolecules* **1991**, *24*, 6660–6663.

(74) Fitzgerald, J. M.; Narang, P.; Craster, R. V.; Maier, S. A.; Giannini, V. *Proc. IEEE* **2016**, *PP*, 1–16.

Supporting Information

Low-loss Plasmonic Dielectric Nanoresonators

Yi Yang,[*,†] Owen D. Miller,[*,‡] Thomas Christensen,[†] John D. Joannopoulos,[†] and Marin Soljačić[†]

†*Research Laboratory of Electronics, Massachusetts Institute of Technology, Cambridge, Massachusetts 02139, USA*

‡*Department of Applied Physics, Yale University, New Haven, CT 06520, USA*

E-mail: yiy@mit.edu; owen.miller@yale.edu

S1 Bulk material parameters

Throughout (with the exception of nonlocal calculations, see below), the material permittivity data of Ag *films* and *nanoparticles* are from Wu *et al.*[1] and Palik[2], respectively throughout the Letter. Material loss of Ag is smaller in Wu *et al.*[1] than in Palik[2]. We adopt these distinct material parameters for distinct regions to reflect the fact that single-or polycrystalline metallic films exhibit much lower losses than metallic nanoparticles (which are typically amorphous, with more severe surface roughness), as we also stated in the maintext. The material permittivity data of Si and Au are from Palik[2]. The permittivity of TiO_2 is from Kim[3]. In all cases, both real and imaginary dispersions are included.

In the nonlocal calculations, Ag is modelled by Drude parameters (see Supporting Info Sec. S9).

S2 Spherical harmonics decomposition

The scattering cross-section of an arbitrarily-shaped isolated scatterer in free space can be decomposed into spherical harmonics. Proper design can spectrally align decoupled channels that gives rise to super-scattering[4]. The scattered field can be projected onto a bounding sphere with radius r around the scatterer, with the scattered electric and magnetic field being $\mathbf{E}_{\text{sca}}$ and $\mathbf{H}_{\text{sca}}$. The electric and magnetic multipole coefficients are[5]

$$a_{lm}^{E} = \frac{(-i)^{l+1}kr}{h_l^{(1)}(kr)E_0[\pi(2l+1)(l+1)]^{1/2}} \int_0^{2\pi}\int_0^{\pi} Y_{lm}^{*}(\theta,\phi)\hat{\mathbf{r}}\cdot\mathbf{E}_{\text{sca}}(\mathbf{r})\sin\theta\,\mathrm{d}\theta\,\mathrm{d}\phi, \tag{S1}$$

$$a_{lm}^{H} = \frac{(-i)^{l}Zkr}{h_l^{(1)}(kr)E_0[\pi(2l+1)(l+1)]^{1/2}} \int_0^{2\pi}\int_0^{\pi} Y_{lm}^{*}(\theta,\phi)\hat{\mathbf{r}}\cdot\mathbf{H}_{\text{sca}}(\mathbf{r})\sin\theta\,\mathrm{d}\theta\,\mathrm{d}\phi, \tag{S2}$$

where Y_{lm} is the scalar spherical harmonics, $h_l^{(1)}$ is the Hankel function of the first kind, k is the wavevector, E_0 is amplitude of the incident field, and Z is the impedance of the ambient

medium. The scattering cross-section is then given by[5]

$$\sigma_{\mathrm{sca}} = \frac{\pi}{k^2} \sum_{l=1}^{\infty} \sum_{m=-l}^{m=l} (2l+1)[|a_{lm}^{E}|^2 + |a_{lm}^{H}|^2], \tag{S3}$$

and the terms in the summation are the contributions from different channels. Due to the azimuthal symmetry of the nanodisk, $|a_{l,m}^{E(H)}| = |a_{l,-m}^{E(H)}|$.

We note that the spherical harmonics decomposition is no longer suitable for a scatterer situated on a substrate, as there is no well-defined bounding sphere around the scatterer. Moreover, there are also scattered guided waves that are not captured by spherical harmonics. Instead, a decomposition into radiative waves and guided waves should be adopted.

S3 Scattering upper bound for a scatterer near a substrate

Here we briefly present a schematic derivation for the upper bound of the scattering cross-section of a nanoparticle on or near a substrate. Ref.[6] already lays out how to derive such bounds for the combined nanoparticle–substrate system; here, we simply show how one can partition the system and bound the nanoparticle's individual contribution.

The key is to define the "incident" and "scattered" fields appropriately. Instead of defining the incident field as a plane wave in free space, and the scattered field as the field arising from the introduction of the nanoparticle and substrate, we instead define the incident field as the field of the plane wave interacting only with the substrate, and the scattered field as the field that arises only once the nanoparticle is added. If χ_{s} is the substrate susceptibility and χ_{p} is the nanoparticle susceptibility, and $H_{\mathrm{vol}}(\mathbf{r})$ is the Heaviside function that is zero everywhere except in the volume *vol*, where it is one, then the incident and scattered fields

are solutions of

$$\left[\nabla\times\nabla\times-\frac{\omega^2}{c^2}\left(1+\chi_{\mathrm{s}}H_{\mathrm{s}}(\mathbf{r})\right)\right]\mathbf{E}_{\mathrm{inc}} = 0 \tag{S4}$$

$$\left[\nabla\times\nabla\times-\frac{\omega^2}{c^2}\left(1+\chi_{\mathrm{p}}H_{\mathrm{p}}(\mathbf{r})\right)\right]\mathbf{E}_{\mathrm{sca}} = \frac{\omega^2}{c^2}\chi_{\mathrm{p}}H_{\mathrm{p}}(\mathbf{r})\mathbf{E}_{\mathrm{inc}} \tag{S5}$$

subject to appropriate (radiation and plane-wave source) boundary conditions. The total field $\mathbf{E}=\mathbf{E}_{\mathrm{inc}}+\mathbf{E}_{\mathrm{sca}}$ is the solution for the total nanoparticle–substrate system. Then we can define the absorbed and scattered powers with respect to only the nanoparticle volume V_{p} and its bounding surface S_{p}:

$$P_{\mathrm{abs}} = \frac{\varepsilon_0\omega}{2}\int_{V_{\mathrm{p}}}\left(\operatorname{Im}\chi_{\mathrm{p}}\right)|\mathbf{E}|^2\,\mathrm{d}V \tag{S6}$$

$$P_{\mathrm{sca}} = \frac{1}{2}\operatorname{Re}\int_{S_{\mathrm{p}}}\mathbf{E}_{\mathrm{sca}}\times\mathbf{H}^*_{\mathrm{sca}}\,\mathrm{d}V. \tag{S7}$$

Despite the perhaps unconventional definition of the "incident" and "scattered" fields, one can prove that the absorbed and scattered powers are positive. The absorbed power P_{abs} is clearly positive, and the scattered power P_{sca} can be proven positive by using the divergence theorem, to the *exterior* of the nanoparticle, which is simply the power radiated by the currents excited within the nanoparticle subject to the plane-wave-plus-substrate incident field. Given the positivity, a straightforward application of the bound approach presented in Ref.[6] leads to bounds identical in form to Eq. (58a) of Ref.[6], with an additional ratio of the average intensity of the new incident field (I_{inc}) to the intensity of a plane wave in free space (I_0):

$$\frac{\sigma_{\mathrm{sca}}}{V}\leq\eta\left(1-\eta\right)k\frac{|\chi|^2}{\operatorname{Im}\chi}\frac{I_{\mathrm{inc}}}{I_0}. \tag{S8}$$

The radiative efficiency η is defined as the ratio between radiative and total decay rates[7]

$$\eta \equiv \frac{\gamma_{\mathrm{rad}}}{\gamma_{\mathrm{tot}}} = \frac{\sigma_{\mathrm{sca}}}{\sigma_{\mathrm{sca}} + \sigma_{\mathrm{abs}}}. \tag{S9}$$

The ratio I_{inc}/I_0 is given by an integral over the volume of the nanoparticle

$$\frac{I_{\mathrm{inc}}}{I_0} = \frac{1}{V_{\mathrm{p}}} \int_{V_{\mathrm{p}}} \frac{|\mathbf{E}_{\mathrm{inc}}|^2}{|\mathbf{E}_0|^2}\, \mathrm{d}V. \tag{S10}$$

For the particle–substrate system, we can write $\mathbf{E}_{\mathrm{inc}} = \hat{\mathbf{x}} \left[e^{ikz} + r_\perp e^{-ikz}\right]$, where $r_\perp$ is the reflection coefficient from the substrate. Then the integral of the incident-field intensity is:

$$\begin{aligned} \int_{V_{\mathrm{p}}} |\mathbf{E}_{\mathrm{inc}}|^2 &= \int_g^{g+h} |e^{ikz} + r_\perp e^{-ikz}|^2\, \mathrm{d}z \\ &= 1 + |r_\perp|^2 \\ &+ \operatorname{Re} r_\perp \frac{\sin 2k(g+h) - \sin 2kg}{kh} - \operatorname{Im} r_\perp \frac{\cos 2k(g+h) - \cos 2kg}{kh}, \end{aligned} \tag{S11}$$

where g and h are the gap size and height of the particle, respectively.

S4 Scattering and absorption of the entire particle-substrate system and of the particle alone

Scattering and absorption cross-sections of the entire particle-substrate system, and of the particle alone, can be explicitly separated.

For the entire system, the scattering cross-section can be obtained by taking a surface integral of the Poynting vector $\mathbf{S}$ of the scattered field on a enclosed surface Ω that also penetrates the substrate

$$\sigma_{\mathrm{sca}} = \frac{1}{2I_0} \int_\Omega \hat{\mathbf{n}} \cdot \mathrm{Re}(\mathbf{S})\, \mathrm{d}\Omega, \tag{S12}$$

where $\hat{\mathbf{n}}$ is the unit vector pointing out of the surface and I_0 is the source intensity. The scattering cross-section includes the excitation of plasmons and photons. A volume integral on the loss per volume inside the particle and the substrate is calculated to extract the absorption cross-section of the whole system

$$\sigma_{\mathrm{abs}} = \frac{\omega}{2I_0} \int_{V_\mathrm{p}+V_\mathrm{s}} \mathrm{Im}\, \varepsilon |\mathbf{E}|^2 \, \mathrm{d}V, \tag{S13}$$

where V_p and V_s are volumes of the particle and substrate, respectively. Note that substrate volume refers to the part of the substrate that is in the vicinity of the particle, such that the local absorption of the *resonances* is captured, rather than the parasite absorption of the propagating plasmons.

For the particle itself, as we described in Section S2, its absorption cross-section can be obtained by calculating the integral shown in Eq. S13 only in V_p

$$\sigma'_{\mathrm{abs}} = \frac{\omega}{2I_0} \int_{V_\mathrm{p}} \mathrm{Im}\, \varepsilon |\mathbf{E}|^2 \, \mathrm{d}V. \tag{S14}$$

The extinction of the particle is given by[6]

$$\sigma'_{\mathrm{ext}} = \frac{\omega}{2I_0} \mathrm{Im} \int_{V_\mathrm{p}} \mathbf{E}^*_{\mathrm{inc}} \cdot \mathbf{P} \, \mathrm{d}V, \tag{S15}$$

where $\mathbf{E}_{\mathrm{inc}} = \hat{\mathbf{x}} \left[e^{ikz} + r_\perp e^{-ikz} \right]$ and $\mathbf{P}$ is the polarizability induced in the particle. The scattering cross-section from the particle can be obtained as $\sigma'_{\mathrm{sca}} = \sigma'_{\mathrm{ext}} - \sigma'_{\mathrm{abs}}$.

S5 Bound-saturated scattering realized via silicon nanorod on a silver film

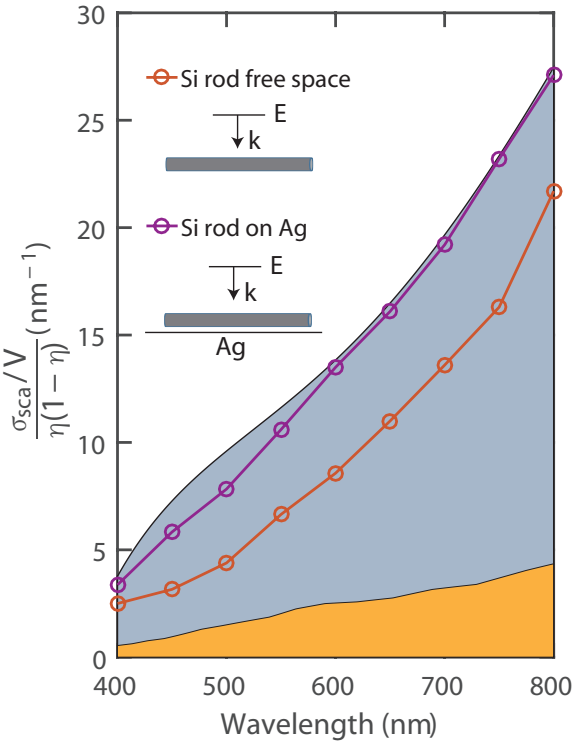

Figure S1: A high-aspect-ratio silicon nanorod on a silver film approaches bound-limited (silicon dictated) scattering strength across visible frequencies while a free-space silicon nanorod fall short. The shaded blue and orange area denote achievable scattering strength for Si and Ag, respectively.

As shown in Fig. S1, in the visible regime, the architecture of a high-aspect-ratio silicon nanorod on a silver film fully saturates the achievable scattering strength, which is dictated by the material properties of silicon, while a free-space silicon nanorod falls short. The shaded regions are the achievable $\mathrm{FOM}_{\mathrm{sca}}$ for silicon (blue) and silver (orange) calculated via Eq. 2. In the Si–Ag structure, the gap size is fixed at 10 nm and the height of the nanorod in tuned such that $I_{\mathrm{inc}} = I_0$ in Eq. 2. Hence, the silicon particle in Si–Ag structure and in free space share the same bound. The resonant wavelength can be tuned by changing the length of the nanorod.

S6 Confinement and dissipative loss of dielectric-dielectric-metal (DDM) and metal-dielectric-metal (MDM) waveguides

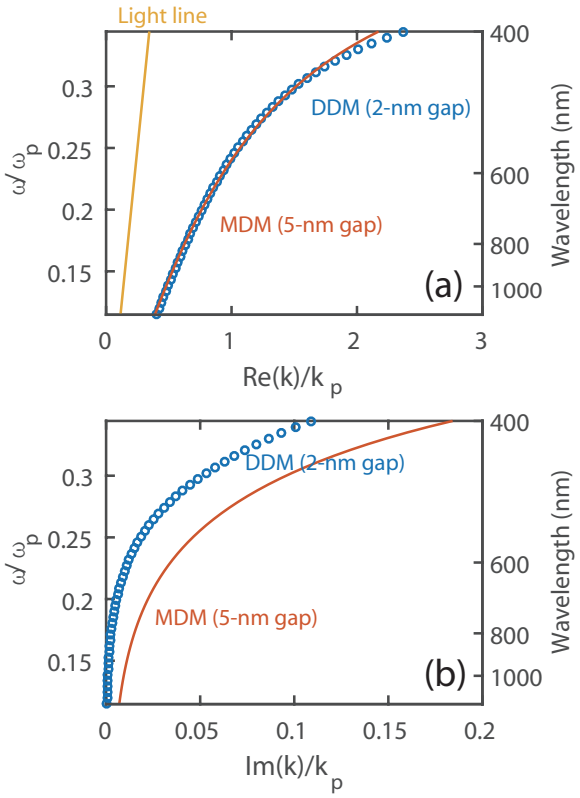

Figure S2: Dispersion of a DDM (Si-Air-Ag) and a MDM (Ag-Air-Ag) waveguide. Same confinement is achieved within the air (a) while loss is greatly mitigated in the DDM waveguide.

In Fig. S2 we show the comparisons of the highly confined plasmon dispersions in a Si-Air-Ag waveguide (2-nm gap) and that in a Ag-Air-Ag waveguide (5-nm gap). The real part of the plasmon wavevectors overlaps [Fig. S2(a)] within the frequency range of interest, indicating the similar local density of states offered from the two structures. On the contrary, the imaginary parts of the wavevectors exhibit sharp contrast, as the Si-Air-Ag waveguide shows much lower loss. Recall the physical picture (Fig. 2) that the localized resonances are created via truncating the superstrate of the waveguide, the hybrid resonances with a 2-nm

gap should offer the similar Purcell enhancement as that of the metal-metal resonance with a 5-nm gap, but equipped with much higher quantum efficiency.

S7 Decomposition and far-field patterns of plasmon and photon emission

The decomposition of photon and plasmon radiation in the entire emission and their corresponding far-field diagrams are computed using a method based on reciprocity arguments using a freely available software package[8]. The near field near the nanoparticle is obtained numerically. For photon radiation, the upper and lower half spaces (with respect to the substrate) are discretized into grids labelled by $(\mathbf{k}, \theta, \phi)$. Mode amplitudes of free-space plane waves are obtained by inner products between the near-field profiles and $e^{i\mathbf{kr}}$. For plasmon radiation, the mode profiles and wavevector k_{spp} of the plasmon is calculated analytically. The xy plane is again discretized into grids labelled by $(\mathbf{k}_{\text{spp}}, \phi)$. Thus, the mode amplitudes of guided plasmons can be obtained by their inner products with the near field. The total photon and plasmon radiation can be calculated by integrating the far-field intensity over all angles.

S7.1 Spontaneous emission enhancement at infrared frequencies

The spontaneous emission enhancement of an antenna is proportional to the local density of states, which is also proportional to the material enhancement factor $|\chi|^2/\text{Im}\chi$[6]. At infrared frequencies, the factor can be one order of magnitude larger than that in the optical regime, leading to a larger Purcell factor and even higher efficiency, as shown in Fig. S3. Combined with the good directionality [Fig. 4(c)], these dielectric-metal resonances are especially ideal for single photon sources[10].

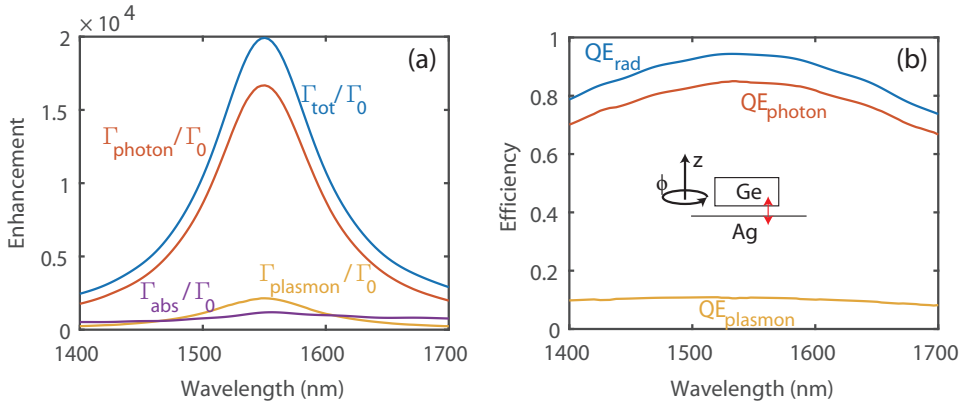

Figure S3: Spontaneous emission enhancement at the telecommunication wavelength using the dielectric-metal resonance. A Purcell factor of 20000 is achieved with a radiative efficiency $\sim$ 95% and a photon efficiency of $\sim$85%. Inset shows the geometry of the structure: a germanium[9] cylinder with radius $r = 135$ nm and height $h = 160$ nm on top of a semi-infinite silver film. The dipole emitter is located at $x = 108$ nm and at the center of the 2-nm gap.

S7.2 Non-vacuum spacer

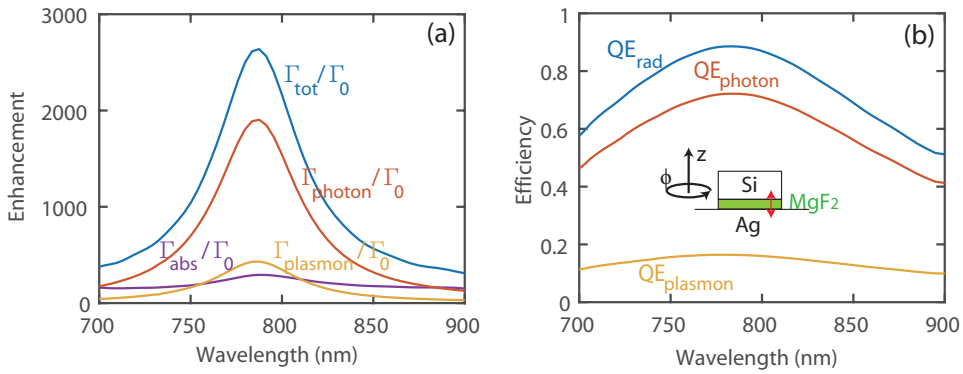

Figure S4: Spontaneous emission enhancement of the dielectric-metal resonance at optical frequencies with a MgF_2 (index $\sim$ 1.375) spacer. A Purcell factor of 2600 is achieved with a radiative efficiency $> 90\%$ and a photon efficiency of $> 70\%$. Inset shows the geometry of the structure: a silicon cylinder with radius $r = 72$ nm and height $h = 100$ nm on top of a semi-infinite silver film. The dipole emitter is located at $x = 60$ nm and at the center of the 2-nm MgF_2 gap.

When the $n = 1$ spacer is replaced with a bulk material, such as a representative low-index dielectrics MgF_2 (index $\sim$ 1.375), the confinement of the localized plasmon becomes worse, leading to a reduced Purcell factor [Fig. S4(a)]. However, the high quantum and photon efficiencies of the emission is maintained [Fig. S4(b)]. As we have highlighted in

the discussion, there are many new types of artificial materials that offer optical indices much lower than those of the natural bulk materials. These artificial materials, such as the low-index SiO_2[11] (index ≈ 1), aerogels[12] (index ≈ 1), and low-index polymers[13], are good candidates for the spacing layer.

S8 Quality factor decomposition

The total quality factor Q_{tot} is obtained via axis-symmetric eigenfrequency calculation (COMSOL), i.e., $Q_{\text{tot}} = \text{Re}\,\omega/2\,\text{Im}\,\omega$. The radiative and absorptive quality factors (Q_{rad} and Q_{abs}) of the resonances are obtained consequently via near-field dipole excitations (Lumerical). The total ($\Gamma_{\text{tot}}/\Gamma_0$) and radiative ($\Gamma_{\text{rad}}/\Gamma_0$) enhancements are obtained by integrating the Poynting vector around the dipole emitter and around the particle, respectively. As there are spectral overlaps among the resonances [Fig. 5(c)] (although resonant peaks are well separated), we adopt a summation of Lorentzian oscillator fitting to extract the decay rates of each individual resonances (Γ^i_{rad} and Γ^i_{abs})[7]

$$\Gamma_{\text{tot}}/\Gamma_0 = \sum_i \frac{\Gamma^i_{\text{tot}}/\Gamma_0}{(\omega-\omega_i)^2+\Gamma^2_{\text{tot}}}, \tag{S16}$$

$$\Gamma_{\text{rad}}/\Gamma_0 = \sum_i \frac{\Gamma^i_{\text{rad}}/\Gamma_0}{(\omega-\omega_i)^2+\Gamma^2_{\text{tot}}}. \tag{S17}$$

Combining Eqs. S16 and S17 with $\Gamma^i_{\text{abs}} = \Gamma^i_{\text{tot}} - \Gamma^i_{\text{rad}}$, one can ready decompose the already-known Q_{tot} into Q_{rad} and Q_{abs}.

S9 Generalized nonlocal optical response

We adopt the generalized nonlocal optical response (GNOR) theory[14,15] to account for quantum effects in the Ag nanoantenna and substrate: this treatment of Ag has been shown to yield results in good agreement with experiment[16–18], despite its neglect of e.g. spill-out and

its essentially phenomenological account of the mechanisms leading to Kreibig damping—in effect, by virtue of error cancellation. The GNOR model adds a convective and diffusive term to the conventional local constitutive equations between the induced current density $\mathbf{J}(\mathbf{r},\omega)$ and the electric field $\mathbf{E}(\mathbf{r},\omega)$. Jointly with Maxwell's equation, this produces the following set of coupled equations:

$$\nabla\times\nabla\times\mathbf{E}(\mathbf{r},\omega)=\frac{\omega^2}{c^2}\varepsilon_\infty\mathbf{E}(\mathbf{r},\omega)+\mathrm{i}\omega\mu_0\mathbf{J}(\mathbf{r},\omega), \tag{S18a}$$

$$\frac{\xi^2}{\omega(\omega+\mathrm{i}\gamma)}\nabla[\nabla\cdot\mathbf{J}(\mathbf{r},\omega)]+\mathbf{J}(\mathbf{r},\omega)=\sigma(\omega)\mathbf{E}(\mathbf{r},\omega), \tag{S18b}$$

with Drude conductivity $\sigma(\omega)=\mathrm{i}\varepsilon_0\omega_\mathrm{p}^2/(\omega+\mathrm{i}\gamma)$ and permittivity $\varepsilon(\omega)=\varepsilon_\infty+\mathrm{i}\sigma/(\varepsilon_0\omega)$. The GNOR parameter ξ sums the contributions of convective (hydrodynamic account of Fermi pressure) and diffusive (phenomenological Kreibig damping) corrections

$$\xi^2=\beta^2+D(\gamma-\mathrm{i}\omega), \tag{S19}$$

with $\beta^2=\frac{3}{5}v_\mathrm{F}^2$ (Fermi velocity, $v_\mathrm{F}=1.39\times10^6$ m/s) and $D=9.62\times10^{-4}$ m^2/s (corresponding to a Kreibig prefactor $A=1$) for Ag[15]. The coupled differential equations of Eqs. (S18) are of higher order than their local counterparts: consequently, an additional boundary condition, $\hat{\mathbf{n}}\cdot\mathbf{J}=0$ (ensuring charge conservation), is necessary for definiteness.

This nonlocal, effective description of quantum corrections in plasmonic Ag nanostructures is representative of the experimental reality, provided adjoining surfaces are sufficiently separated that quantum tunnelling at optical frequencies is negligible—an effect which requires gaps $\lesssim 0.5$ nm[19]—and provided the characteristic geometric feature-sizes remain $\gtrsim 1$ nm. For the structures studied in this Letter, these conditions are rigorously fulfilled.

S9.1 Bulk material parameters for GNOR calculations

We adopt a simple Drude-description of Ag's permittivity (i.e., we ignore spectral dispersion in ε_∞):

$$\varepsilon = \varepsilon_\infty - \frac{\omega_\mathrm{p}^2}{\omega(\omega + \mathrm{i}\gamma)}. \tag{S20}$$

Specifically, for the Ag *film* we take $\varepsilon_\infty = 3.3$, $\omega_\mathrm{p} = 1.35 \times 10^{16}$ rad/s, and $\gamma = 3.34 \times 10^{13}$ rad/s, matching the state-of-the-art material qualities attainable in Ag films[1,20,21]. In Ag *nanoparticles* we adopt the same values, except for an increased decay-rate $\gamma = 1.40 \times 10^{14}$ rad/s[2]. This distinction reflects the fact that metallic films, fabricated e.g. by low-temperature epitaxial-growth[1] or by high-temperature sputtering[21], have significantly lower Ohmic losses than that attainable in nanoparticles because of their higher crystallinity and lower surface roughness.

The Si nanoparticles are, as noted in the Letter, treated in a local framework, with material properties from Ref.[2]. We emphasize that a local treatment of Si is justified, given the bound nature of the electrons which contribute to the optical properties of Si in the considered frequency range.

S9.2 Numerical simulations of nanoparticle–substrate system

The calculations depicted in Fig. 6 are performed using COMSOL, achieved by numerically solving Eqs. (S18a) and (S18b) self-consistently. We exploit the structure's rotational symmetry by decomposing the incident plane waves in cylindrical harmonics which allows us to calculate the near-field properties for each azimuthal index m separately. As our focus is on the lowest order $(1, 1)$ resonance, we restrict our considerations to the $m = 1$ channel. This reduces the dimensionality of the computational problem from three to two, allowing significant reductions in computational time and memory requirements.

S9.3 Nonlocal effects in planar waveguide structures

As noted in the main text, the underlying planar three-layer waveguide approximately dictates the gap-dependence of the nanoparticle on a substrate architecture, also with respect to nonlocal effects. For this reason, we discuss here the planar three-layer waveguide (assumed translation invariant in the xy-plane) in the context of a simple hydrodynamic (i.e. $D = 0$ and $\beta \neq 0$) model. We consider two distinct setups: (i) a metal–dielectric–metal (MDM) waveguide, built from top-and-bottom layers of a simple metal (Wigner–Seitz radius $r_s = 3$; corresponding to a lossless Drude metal of plasma frequency $\omega_\mathrm{p} = 9.0705$ eV), separated by a vacuum gap of extent g, and (ii) a dielectric–dielectric–metal (DDM) waveguide, consisting of a bottom layer of a simple metal ($r_s = 3$), a vacuum gap of extent g, and a top layer of non-unity permittivity $\varepsilon = 3.5$[2].

Figure S5(a) presents the dispersion of the E_z-symmetric (antisymmetric potential) plasmon mode of the MDM and DDM waveguides in both local and nonlocal treatments for three gap-sizes, obtained by numerically solving the retarded dispersion equations[22]. The spectral deviation between local and nonlocal treatments, $\delta\omega_\mathrm{local}^\mathrm{nonlocal} \equiv \omega_\mathrm{nonlocal} - \omega_\mathrm{local}$, is further examined in Fig. S5(b): the MDM waveguide exhibits larger nonlocal corrections than its DDM counterpart throughout. Working in a nonretarded framework[23], the spectral deviation can be well-approximated by a leading-order treatment in $\beta k/\omega_\mathrm{local} \ll 1$, allowing the following analytical approximations for the MDM and DDM waveguides:

$$\delta\omega_\mathrm{local}^\mathrm{nonlocal}\big|_\mathrm{MDM} \simeq \tfrac{1}{2}\beta k\sqrt{\frac{1+\mathrm{e}^{-kg}}{1-\mathrm{e}^{-kg}}} + \mathcal{O}[(\beta k)^2], \tag{S21a}$$

$$\delta\omega_\mathrm{local}^\mathrm{nonlocal}\big|_\mathrm{DDM} \simeq \tfrac{1}{2}\beta k\sqrt{\frac{(\varepsilon+1)+(\varepsilon-1)\mathrm{e}^{-2kg}}{(\varepsilon+1)-(\varepsilon-1)\mathrm{e}^{-2kg}}} + \mathcal{O}[(\beta k)^2]. \tag{S21b}$$

These approximate analytical expressions agree well with the fully retarded numerical results, see Fig. S5(b), particularly for $kg \ll 1$ and $k \gg \sqrt{\varepsilon}\omega/c$. Moreover, they allow the synthesis of a simple estimate of the relative impact of nonlocality—and, more broadly, any surface-

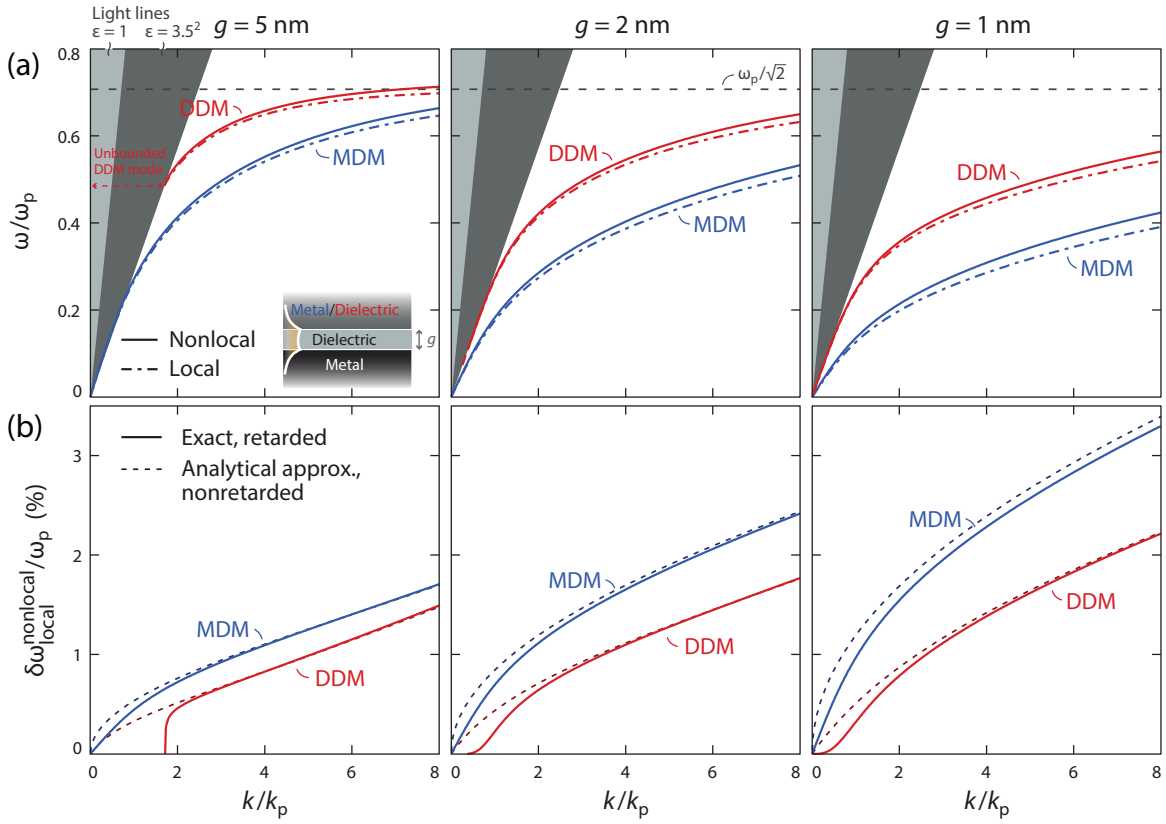

Figure S5: Low-energy plasmon modes of MDM and DDM waveguides (defined in text) in local and nonlocal treatments, across three gap-sizes. (a) Frequency dispersion with wave vector k. Only modes which are bound in both bottom and *top* layers are depicted. (b) The spectral deviation $\delta\omega_{\rm local}^{\rm nonlocal}$ between local and nonlocal treatments. Unbound (i.e. radiating) DDM modes suffer no nonlocal correction. Nonretarded, leading-order approximations, i.e. Eqs. (S21), agree well with the full, retarded calculations. In all cases, the DDM suffers less nonlocal correction than the MDM.

related quantum corrections[23]—by their ratio:

$$\frac{\delta\omega_{\rm local}^{\rm nonlocal}\big|_{\rm MDM}}{\delta\omega_{\rm local}^{\rm nonlocal}\big|_{\rm DDM}} \simeq \sqrt{\frac{1+{\rm e}^{-kg}}{1-{\rm e}^{-kg}}\Big/\frac{(\varepsilon+1)+(\varepsilon-1){\rm e}^{-2kg}}{(\varepsilon+1)-(\varepsilon-1){\rm e}^{-2kg}}} \simeq 1+{\rm e}^{-kg}-\frac{1}{2}\frac{\varepsilon-3}{\varepsilon+1}{\rm e}^{-2kg}, \qquad \text{(S22)}$$

with the last step assuming $kg \gg 1$. These results demonstrate that the DDM waveguide is less impacted by nonlocal corrections than the MDM waveguide; in turn, the dielectric nanoparticle architecture inherits this favorable aspect. In concert with a reduced nonlocal penalty due to the absence of sharp metallic edges, this facilitates the dielectric nanoparticle architecture's superior robustness to gap-dependent quantum-corrections (relative to its all-

metallic counterpart), as discussed in main text.

References

(1) Wu, Y.; Zhang, C.; Estakhri, N. M.; Zhao, Y.; Kim, J.; Zhang, M.; Liu, X.-X.; Pribil, G. K.; Alù, A.; Shih, C.-K.; Li, X. *Adv. Mater.* **2014**, *26*, 6106–6110.

(2) Palik, E. D. *Handbook of optical constants of solids*; Academic press, 1998; Vol. 3.

(3) Kim, S. *Appl. Opt.* **1996**, *35*, 6703–6707.

(4) Ruan, Z.; Fan, S. *Phys. Rev. Lett.* **2010**, *105*, 013901.

(5) Kong, J. *Electromagnetic Waves Theory*; EMW Publishing, Cambridge, MA, 2005.

(6) Miller, O. D.; Polimeridis, A. G.; Reid, M. H.; Hsu, C. W.; DeLacy, B. G.; Joannopoulos, J. D.; Soljačić, M.; Johnson, S. G. *Opt. Express* **2016**, *24*, 3329–3364.

(7) Hamam, R. E.; Karalis, A.; Joannopoulos, J. D.; Soljačić, M. *Phys. Rev. A* **2007**, *75*, 053801.

(8) Yang, J.; Hugonin, J.-P.; Lalanne, P. *ACS Photon.* **2016**, *3*, 395–402.

(9) Tauc, J.; Abraham, A. *Czechoslovak Journal of Physics B* **1969**, *19*, 1246–1254.

(10) Aharonovich, I.; Englund, D.; Toth, M. *Nat. Photon.* **2016**, *10*, 631–641.

(11) Xi, J.-Q.; Schubert, M. F.; Kim, J. K.; Schubert, E. F.; Chen, M.; Lin, S.-Y.; Liu, W.; Smart, J. A. *Nat. Photon.* **2007**, *1*, 176–179.

(12) Sun, Y.; Forrest, S. R. *Nat. Photon.* **2008**, *2*, 483–487.

(13) Groh, W.; Zimmermann, A. *Macromolecules* **1991**, *24*, 6660–6663.

(14) Mortensen, N. A.; Raza, S.; Wubs, M.; Søndergaard, T.; Bozhevolnyi, S. I. *Nat. Commun.* **2014**, *5*, 3809.

(15) Raza, S.; Bozhevolnyi, S. I.; Wubs, M.; Mortensen, N. A. *J. Phys.: Condens. Matter* **2015**, *27*, 183204.

(16) Raza, S.; Stenger, N.; Kadkhodazadeh, S.; Fischer, S. V.; Kostesha, N.; Jauho, A.-P.; Burrows, A.; Wubs, M.; Mortensen, N. A. *Nanophotonics* **2013**, *2*, 131–138.

(17) Raza, S.; Kadkhodazadeh, S.; Christensen, T.; Di Vece, M.; Wubs, M.; Mortensen, N. A.; Stenger, N. *Nature Commun.* **2015**, *6*.

(18) Charlé, K.-P.; König, L.; Nepijko, S.; Rabin, I.; Schulze, W. *Cryst. Res. Technol.* **1998**, *33*, 1085–1096.

(19) Yan, W.; Wubs, M.; Mortensen, N. A. *Phy. Rev. Lett.* **2015**, *115*, 137403.

(20) Johnson, P. B.; Christy, R.-W. *Phys. Rev. B* **1972**, *6*, 4370.

(21) McPeak, K. M.; Jayanti, S. V.; Kress, S. J.; Meyer, S.; Iotti, S.; Rossinelli, A.; Norris, D. J. *ACS Photon.* **2015**, *2*, 326–333.

(22) Raza, S.; Christensen, T.; Wubs, M.; Bozhevolnyi, S. I.; Mortensen, N. A. *Phys. Rev. B* **2013**, *88*, 115401.

(23) Christensen, T.; Yan, W.; Jauho, A.-P.; Soljačić, M.; Mortensen, N. A. *Phys. Rev. Lett.* **2017**, *118*, 157402.